



A geometric framework for channel network extraction from lidar: Nonlinear diffusion and geodesic paths

Paola Passalacqua,¹ Tien Do Trung,² Efi Foufoula-Georgiou,¹ Guillermo Sapiro,³ and William E. Dietrich⁴

Received 21 January 2009; revised 30 July 2009; accepted 4 September 2009; published 7 January 2010.

[1] A geometric framework for the automatic extraction of channels and channel networks from high-resolution digital elevation data is introduced in this paper. The proposed approach incorporates nonlinear diffusion for the preprocessing of the data, both to remove noise and to enhance features that are critical to the network extraction. Following this preprocessing, channels are defined as curves of minimal effort, or geodesics, where the effort is measured on the basis of fundamental geomorphological characteristics such as flow accumulation area and isoheight contours curvature. The merits of the proposed methodology, and especially the computational efficiency and accurate localization of the extracted channels, are demonstrated using light detection and ranging (lidar) data of the Skunk Creek, a tributary of the South Fork Eel River basin in northern California.

Citation: Passalacqua, P., T. Do Trung, E. Foufoula-Georgiou, G. Sapiro, and W. E. Dietrich (2010), A geometric framework for channel network extraction from lidar: Nonlinear diffusion and geodesic paths, *J. Geophys. Res.*, 115, F01002, doi:10.1029/2009JF001254.

1. Introduction

[2] The detection of channel networks and the localization of channel heads from digital elevation (DEM) data are fundamental to the accurate modeling of water, sediment, and other environmental fluxes in a watershed. Several methodologies to delineate channel heads and channel networks from DEMs have been proposed [e.g., *Montgomery and Dietrich*, 1988; *Tarboton et al.*, 1988, 1991; *Montgomery and Foufoula-Georgiou*, 1993; *Costa-Cabral and Burges*, 1994; *Giannoni et al.*, 2005; *Hancock and Evans*, 2006]. Channel heads typically are found in unchanneled valleys and appear to occur where some erosion threshold has been crossed (e.g., landsliding, overland flow incision through a vegetated surface, seepage erosion, etc.) [e.g., *Montgomery and Dietrich*, 1988; *Dietrich et al.*, 1993]. Field data also show that channel head location varies with a topographic threshold that depends on drainage area and local valley slope [e.g., *Montgomery and Dietrich*, 1988, 1989, 1992, 1994]. More recently, for example, *McNamara et al.* [2006]

located channel heads in a small watershed in Thailand and suggested that different channel initiation processes produced different slope-area relationships. Several studies employ, instead, an assumption of constant critical support area for determining the location of channel heads [e.g., *O'Callaghan and Mark*, 1984; *Band*, 1986; *Mark*, 1988; *Tarboton et al.*, 1989, 1991; *McMaster*, 2002], although empirical support from field observations was not reported. Other work has explored the localization of channel heads by identifying valley heads as concave areas in DEMs [*Tribe*, 1991, 1992].

[3] With the availability of high-resolution topographic data obtained by airborne laser mapping, new methodologies have been proposed for the determination of the locations and distribution of landslide activity [e.g., *McKean and Roering*, 2004; *Glenn et al.*, 2006; *Ardizzone et al.*, 2007; *C. Gangodagamage et al.*, Statistical signature of deep-seated landslides, submitted to *Journal of Geophysical Research*, 2009], the geomorphological mapping of glacial landforms [*Smith et al.*, 2006], numerical modeling of shallow landslides [e.g., *Dietrich et al.*, 2001; *Tarolli and Tarboton*, 2006], computation of channel slope [*Vianello et al.*, 2009], identification of depositional features of alluvial fans [*Staley et al.*, 2006; *Frankel and Dolan*, 2007; *Cavalli and Marchi*, 2008] and of channel bed morphology [*Cavalli et al.*, 2008], and the detection of hillslope-to-valley transition [*Tarolli and Dalla Fontana*, 2009].

[4] Light detection and ranging (lidar) data now permits direct detection of channels, rather than estimation of likely channel location based on topographic features (slope, drainage area, or topographic curvature). Recently, *Lashermes et al.* [2007] proposed a wavelet-based filtering

¹Saint Anthony Falls Laboratory, National Center for Earth Surface Dynamics, Department of Civil Engineering, University of Minnesota, Minneapolis, Minnesota, USA.

²Département de Mathématiques, Ecole Normale Supérieure de Cachan, Paris, France.

³Department of Electrical and Computer Engineering, University of Minnesota, Minneapolis, Minnesota, USA.

⁴Department of Earth and Planetary Science, University of California, Berkeley, California, USA.

methodology to extract channels and channel networks from high-resolution topography that can be obtained from airborne lidar data. In the methodology of *Lashermes et al.* [2007], multiscale analysis, i.e., going from fine to coarser scales, was achieved via a convolution of the original image with a Gaussian kernel at different scales. This is equivalent to applying the heat equation on the image going forward in time (e.g., see *Braunmandl et al.* [2003] and later in this paper). Gaussian linear filtering, however, smoothes small-scale structures at the same rate as it smoothes larger-scale structures (actually some of the most critical scales are smoothed even faster, which can be shown following the theory of robust estimation). This might not be desirable in DEM feature extraction as small-scale structures, such as the crest of a ridge or channel bank, should remain sharp during coarsening until the whole ridge disappears. This problem of edge preservation has prompted in image processing the introduction of adaptive geometric filters which reduce smoothing at the edges of features while applying Gaussian filtering to the rest of the image.

[5] In this paper, a geometric framework which significantly advances the accurate and automatic extraction of channel networks from lidar data is developed using such scale-adaptive filtering. The first component of the framework is the use of nonlinear geometric filtering (via partial differential equations), instead of linear filtering via wavelets, which naturally adapts to a given landscape and facilitates the enhancement of features for further processing. Early uses of nonlinear partial differential equations for digital elevation maps appear in the work of *Braunmandl et al.* [2003], *Almansa et al.* [2002], and *Solé et al.* [2004]. The form of this filtering is such that it behaves as linear diffusion at low-elevation gradients, while it arrests diffusion as the gradients become large (other features could be used to control the nonstationary diffusion as well). It is noted that the nonlinear diffusion term here employed refers to the filtering methodology in image processing and not to the nonlinear erosion laws [e.g., *Kirkby*, 1984, 1985; *Andrews and Buckman*, 1987; *Anderson and Humphrey*, 1989; *Anderson*, 1994; *Howard*, 1994a, 1994b, 1997; *Roering et al.*, 1999]. The second key component of the proposed framework is the novel formulation of the channel network extraction problem as a geodesic energy minimization problem with a cost function which is geomorphologically informed; that is, it is defined in terms of local attributes of the landscape such as upstream drainage area and isoheight contours curvature. In other words, channels are defined as curves of minimal effort. Such curves are derived from global integration of local quantities and computed in optimal linear complexity. This global integration methodology makes the channel network extraction robust to noise and data interruptions, contrary to what obtained with more common forward marching approaches (e.g., following steepest descent directions).

[6] This paper is organized as follows. Section 2 gives a brief mathematical background on nonlinear diffusion, geometric filtering, geodesics, and energy minimization principles. In section 3 these techniques are applied to the problem of channel network extraction and demonstrated in

a real basin. Finally, section 4 presents concluding remarks and challenges for future research.

2. Mathematical Background on the Proposed Methodology

[7] This section presents the basic mathematical background that provides the foundation for the channel network extraction geometric framework introduced in this paper. First, the notion of nonlinear anisotropic filtering is introduced. Next, the framework of geodesic computations is presented. The channel extraction methodology presented here has been released to the community as a toolbox called GeoNet. The code is available for download at <http://software.nced.umn.edu/geonet/>.

2.1. Nonlinear Diffusion and Geometric Filtering

[8] Let us denote by $h_0(x, y): \mathbb{R}^2 \rightarrow \mathbb{R}$ the provided DEM image, i.e., high-resolution digital elevation data. Typical of any feature extraction methodology is the application of a *smoothing* filter on the original data $h_0(x, y)$ to remove “noise” (observational noise or irregularities at scales smaller than the scales of interest) and identify features as entities that persist over a range of scales. This operation of smoothing is also very important to make computations such as derivatives mathematically well posed. A popular smoothing filter is the Gaussian kernel, which, when applied to $h_0(x, y)$, results in landscapes at coarser resolutions:

$$h(x, y, t) = h_0(x, y) \star G(x, y; t) \quad (1)$$

where \star denotes the convolution operation and $G(x, y; t)$ is a Gaussian kernel of standard deviation t (larger values of t result in coarser resolution landscapes), centered at location (x, y) :

$$G_{x,y,t}(u, v) = \frac{1}{2\pi t} \exp\left[-\frac{(u-x)^2 + (v-y)^2}{2t}\right] \quad (2)$$

As it was shown and exploited in the work of *Lashermes et al.* [2007], the use of the classical Gaussian smoothing kernel naturally leads to a multiscale (scale-space in the computer vision terminology) efficient computation of local slopes and Laplacian curvatures via wavelets, where wavelets were selected as the first and second derivatives of a Gaussian kernel (see *Burt and Adelson* [1983], *Koenderink* [1984], and *Witkin* [1983] for early developments and the introduction of Gaussian filtering for multiscale image analysis).

[9] The family of coarsened landscapes resulting from (1) may be seen as solutions of the linear heat or diffusion equation, e.g., see *Koenderink* [1984], with the initial condition $h(x, y, 0) = h_0(x, y)$:

$$\partial_t h(x, y, t) = \nabla \cdot (c \nabla h) = c \nabla^2 h \quad (3)$$

where c is the diffusion coefficient and ∇ is the gradient operator. Thus, processing the landscape with Gaussian

filters of increasing spatial scale, as done by *Lashermes et al.* [2007], is equivalent to applying an isotropic diffusion equation over time on the landscape with the spatial scale of the filter (variance) and the time of diffusion being related to each other (since derivatives are linear operations, filtering and then differentiating is equivalent to filtering with the corresponding derivatives of the original filter; see also *Lashermes et al.* [2007] for a formal exposition). Once the time of diffusion is fixed, the spatial scale over which the Gaussian smoothing is applied on the original landscape is spatially uniform; that is, the landscape is uniformly diffused at all points and in all directions.

[10] The choice of the Gaussian kernel as smoothing filter is motivated in part by two criteria defined by *Koenderink* [1984] as (1) *causality* and (2) *homogeneity/isotropy*. The *causality* guarantees that no spurious feature should be generated at coarser resolutions, since any feature at a coarse level of resolution must have a cause at a finer level of resolution. This guarantees noise reduction in the original data as the resolution is coarsened. The *homogeneity/isotropy* criterion requires the blurring to be space invariant. The Gaussian kernel thus satisfies the standard “scale-space paradigm” as stated by *Koenderink* [1984]. It is noted, however, that the Gaussian filtering is isotropic and does not respect the natural boundaries of the features and diffuses across boundaries throughout the landscape. This obviously degrades the spatial localization of these boundaries, especially at larger scales of smoothing. These boundaries represent, in the case of landscapes, important discontinuities such as crests and valleys. *Perona and Malik* [1990] reformulated the space-scale paradigm to address this issue. The new paradigm was reformulated to satisfy three criteria: (1) *causality*, as previously stated by *Koenderink* [1984], (2) *immediate localization*, which searches, at each resolution, sharp and meaningful region boundaries, and (3) *piecewise smoothing*, which indicates preferential smoothing (intra-region rather than inter-region).

[11] In the standard linear diffusion equation (3), the diffusion coefficient c is constant, that is, independent of the space location. An extension to the Gaussian filtering is obtained by choosing the diffusion coefficient c to be a suitable function of spatial location, such that the new space-scale paradigm criteria are satisfied. The modified diffusion equation can be written as

$$\partial_t h(x, y, t) = \nabla \cdot [c(x, y, t) \nabla h] \quad (4)$$

where ∇ indicates as before the gradient operator. Note that (4) reduces to the linear diffusion equation (3) if $c(x, y, t)$ is constant.

[12] If the location of a channel were known, then, in order to achieve noise reduction and edge enhancement, smoothing should preferentially happen in the region outside and within the channel, rather than across its boundary. This could be achieved by setting $c = 0$ at the channel boundaries and $c = 1$ everywhere else. However the channel location is not known in advance, and what can be computed instead is an estimate of it, or some geometric characteristic that defines it, thereby stopping, or at least reducing, diffusion across the channel boundary.

[13] Let $\vec{E}(x, y, t)$ denote the vector-valued function representing an estimate of the channel’s location. The

diffusion coefficient can be chosen as a function of the magnitude of $\vec{E}(x, y, t)$:

$$c = p(|\vec{E}|) \quad (5)$$

where $p(\cdot)$ has to be designed such that it ideally does not allow diffusion across boundaries. *Perona and Malik* [1990] have proposed a simple first estimate of the channel’s location (or image edges in their original application), given by the gradient of the elevation $h(x, y, t)$ at the location (x, y) and time t :

$$\vec{E}(x, y, t) = \nabla h(x, y, t) \quad (6)$$

This provides a local estimator of the edges/discontinuities within the nonlinear space-scale paradigm. Note that we could also use curvature, area in combination with slope, or other higher-order features to localize channels and thus define the diffusion coefficient c , while the use of gradients is the most standard formulation in image processing and found to be sufficient for our application (see also discussion of *Perona and Malik* [1990] for advantages of such a simple formulation). The diffusion equation thus takes the following form:

$$\partial_t h(x, y, t) = \nabla \cdot [p(|\nabla h|) \nabla h] \quad (7)$$

Perona and Malik suggested the following as possible edge-stopping functions:

$$p(|\nabla h|) = \frac{1}{1 + (|\nabla h|/\lambda)^2} \quad (8)$$

or

$$p(|\nabla h|) = e^{-(|\nabla h|/\lambda)^2} \quad (9)$$

where λ is a constant. Such expressions (when properly regularized, e.g., via Gaussian smoothing) of the edge-stopping function guarantee basic properties of the scale-space paradigm, while at the same time enhancing the discontinuities, thereby allowing their easier extraction (see *Alvarez et al.* [1992], *Perona and Malik* [1990], and the Appendix for details). From a numerical point of view, we employ the version of the Perona-Malik filter proposed by *Catté et al.* [1992]. The diffusion coefficient c is computed in the four directions (north, south, east, and west) with the gradients in (8) or (9) computed through standard finite differences on Gaussian filtered data (with a very small standard deviation of the kernel $\sigma = 0.05$ m), to avoid the stability issues related to the Perona-Malik original formulation [*Catté et al.*, 1992]. Then, the gradients in (7) are computed on the nonsmoothed data through standard finite differences, multiplied by the diffusion coefficient in each direction and then summed to advance in time.

[14] The just introduced nonlinear diffusion equation (7) will be used as a preprocessing step on the elevation data, to remove unwanted details and enhance the features that are relevant for channel network extraction. While many alternatives exist in the literature for nonlinear diffusion, we

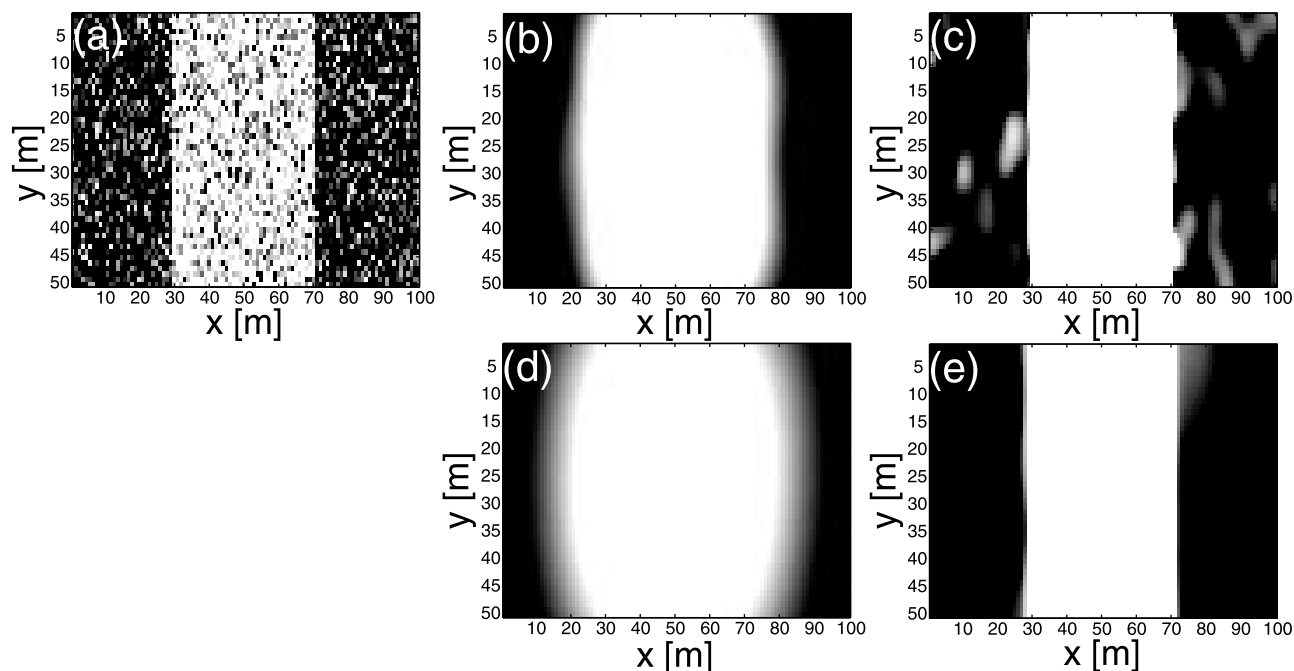


Figure 1. Comparison of the effect of Gaussian (linear) versus Perona-Malik (nonlinear) filtering on an idealized landscape. The white area represents an idealized ridge, with an elevation higher than the surrounding landscape. (a) Noise has been added on the original data. (b) Gaussian filtering achieves noise reduction at the expense of the boundaries localization (standard deviation of the kernel $\sigma = 7$ m), while (c) Perona-Malik filtering achieves noise reduction while preserving the right localization, avoiding diffusion across its boundaries (number of iterations $t = 50$). (d) Note how further processing with Gaussian filtering results in a completely blurred ridge ($\sigma = 14$ m), while (e) the Perona-Malik filtering operation only reduces the noise further, without affecting the feature and its localization ($t = 200$).

found this basic and most classical one to be sufficient to introduce the ideas and to obtain state-of-the-art results for the tested lidar elevation data.

[15] We have constructed an example to show the effect of Gaussian (linear) versus Perona-Malik (nonlinear) filtering on an idealized landscape (Figure 1a) with noise added on the surface. The white band represents an idealized ridge at a higher elevation compared to the surrounding landscape. As shown in Figure 1b Gaussian filtering (standard deviation of the kernel $\sigma = 7$ m which corresponds to $t = \sigma^2 = 49$) achieves noise reduction at the expense of the localization of the ridge, as it appears diffused in the neighboring landscape. The Perona-Malik filter (Figure 1c after $t = 50$ iterations) achieves noise reduction without affecting the boundaries localization. Note how after further processing the idealized landscape through Gaussian filtering (Figure 1d with $\sigma = 14$ m which corresponds to $t = 196$) the ridge and its location are not identifiable anymore, while the Perona-Malik filtering (Figure 1e with $t = 200$) only improves noise reduction, without affecting the feature. In addition Figure 2 shows the profiles extracted from the idealized landscape shown in Figure 1. Figure 2a shows the case of an idealized landscape with no noise added on the surface. Note how the profile extracted from the Perona-Malik filtered data after $t = 50$ iterations resembles the original one, while the idealized ridge has almost disappeared from the Gaussian filtered landscape. The profiles shown in Figures 2b and 2c refer to the same idealized landscape with noise added on the surface shown in

Figure 1. Note how well defined and enhanced appear the ridge after further Perona-Malik filtering of the data. This is due to the fact that at the boundary between the ridge and the surrounding landscape the gradients are large, thus diffusion is stopped.

2.2. Geodesics and Energy Minimization Principles for Network Extraction

[16] Having applied the Perona-Malik filter to the initial DEM image, unwanted details have been eliminated, or reduced, and the features enhanced. The question then arises as to how to best (optimally) extract the whole channel network.

[17] If we have two fixed points a and b on the surface, we know there are infinite possible curves passing through them. If a and b now represent the outlet and a channel head of a tributary river network, then we know that among all the possible curves, only one will be a channel. (The detection of the outlet and of the channel sources will be explained later in section 3.2. For now, let us assume their locations are known). Topographic attributes that distinguish channels from the rest of the landscape are the surface curvature and the flow accumulation. Channelized areas are, in fact, commonly characterized by positive curvature (or curvature above a threshold value which indicates convergent topography, while negative curvature indicates divergent topography correspondent to hillslopes) and by large values of flow accumulation (as channelized paths collect water in the downstream direction). If we were able to

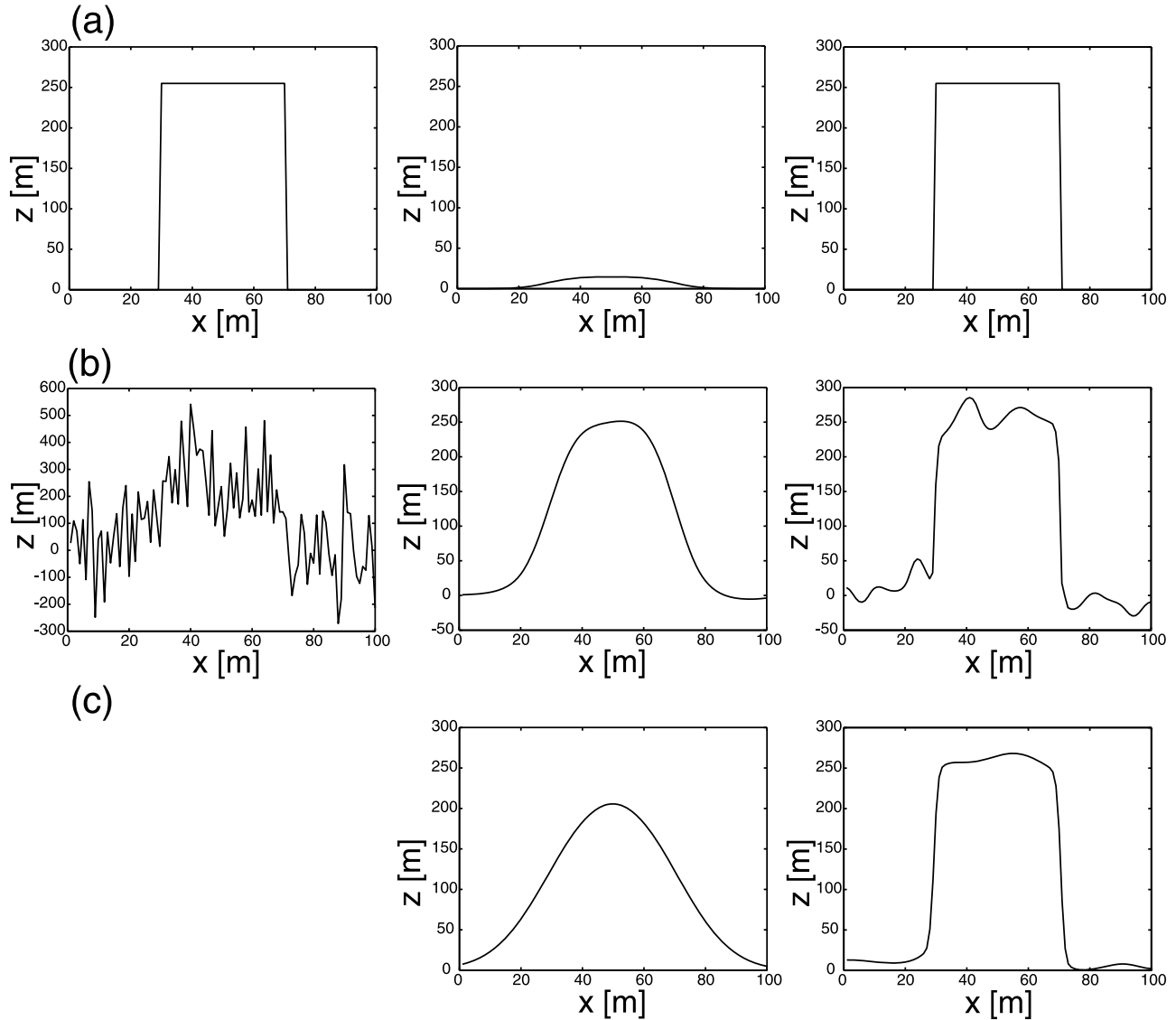


Figure 2. The 1-D representation of the example shown in Figure 1. (a) Idealized landscape with no noise added on the surface. Profiles extracted from the original idealized landscape (left), the Gaussian filtered landscape ($\sigma = 7$ m) (middle), and the Perona-Malik filtered landscape ($t = 50$) (right). (b) Idealized landscape with noise added on the surface as shown in Figure 1. Profiles extracted from the original idealized landscape (left), the Gaussian filtered landscape ($\sigma = 7$ m) (middle), and the Perona-Malik filtered landscape ($t = 50$) (right). (c) Effect of further smoothing on the data shown in Figure 2b. Profiles extracted from the Gaussian filtered landscape ($\sigma = 14$ m) (middle) and Perona-Malik filtered landscape ($t = 200$) (right).

choose among all the possible curves connecting point a and point b (the outlet and a channel head of our river network) the one with the largest overall positive curvature and flow accumulation, then we would have identified the channel. This concept can be mathematically expressed through a function, called the “cost function” and indicated by ψ , which represents the cost of traveling between point a and point b, in this case in terms of surface curvature and flow accumulation. This means that while the channel itself will be the curve with minimum cost (as will meet the requirements of positive curvature and large flow accumulation), the other curves will be penalized with a higher cost. The curve with the minimal cost corresponds to a mathemati-

cally defined quantity called the *geodesic curve* and formally defined as follows:

$$g(a, b) := \arg \left(\min_{C \in \Omega} \int_a^b \psi(s) ds \right) \quad (10)$$

where s is the standard Euclidean arc length [Do Carmo, 1976]. The minimum is taken over all the possible curves C that start at point a and end at point b.

[18] Before we give more details on how the computation of the geodesic curve is performed, let us make two important observations related to the just introduced concepts. First,

having said that for the detection of channels we define the cost function in terms of positive surface curvature and large flow accumulation, implies that different feature selections of the cost function will lead to different curves on the surface. This means that this approach could be used for the detection of other features of interest, such as roads or landslides for example, with the only challenge of being able to identify the most appropriate topographic attributes needed. Also, as it can be seen from equation (10) the integral sign indicates that the minimum is achieved in a global sense, not locally. If, for example, channels were to be traced following steepest descent directions, then the presence of noise in a pixel would deviate the channel in an erroneous way, while the global approach guarantees robustness. The same happens in the case of missing data: while forward marching techniques would stop, global approaches such as the geodesic framework would naturally “jump” over them, as they always connect the selected extreme points.

[19] The computation of the geodesic curve involves another well defined mathematical quantity called *geodesic distance*:

$$d(a, x) := \min_{C \in \Omega} \int_a^x \psi(s) ds \quad (11)$$

This is the quantity which gives us the minimum distance from any point x to location a , computed by minimizing the cost function. Intuitively we can now see how, if we want to travel from point a to point b along the geodesic curve (which in our case it means that we want to identify the channel that connects the outlet and a channel head), we need to use the information given by the geodesic distances. Formally, the actual geodesic curve is computed by gradient descent on the distance function $d(a, \cdot)$, backtracking from the “downstream” point b . The geodesic is thus the integral curve of ∇d starting at point b , and the gradient is intrinsically computed on the surface. Clearly, the efficiency of the computation of the geodesic curves depends on the computation of the geodesic distances. Several algorithms are available in the literature for the efficient computation of the geodesic distances [e.g., *Yatziv et al.*, 2006; *Dial*, 1969; *Dijkstra*, 1959]. These algorithms are applicable to all diverse types of surface representations, from triangulated surfaces [*Kimmel*, 2003] to point cloud data as in lidar [*Memoli and Sapiro*, 2005]. These extensions are based on the fact that the geodesic distance function satisfies a Hamilton-Jacobi geometric partial differential equation, $|\nabla d| = \psi$, where the gradient is intrinsic to the surface in the most general case. Additional information on these efficient computations can be found in the work of *Helmsen et al.* [1996], *Sethian* [1999], *Tsitsiklis* [1995], *Tsai et al.* [2003], and *Zhao* [2004]. Note that these algorithms are of complexity linear on the number of grid points, and thereby computationally optimal.

3. Channel Network Extraction

[20] The objective of this section is to illustrate the concepts described above through their application on lidar data of the South Fork Eel River basin in northern California. We use the ALSM (Airborne Laser Swath Mapping) data

(2.6 m average bare earth data spacing, gridded to 1 m) acquired by NCALM (National Center for Airborne Laser Mapping) (the data are available online at the data distribution archive <http://www.ncalm.org/>). We focus in particular on the Skunk Creek, a 0.54 km² landslide complex tributary located just upstream of the Elder Creek. The subbasin and the location map are shown in Figure 3. For the Skunk Creek we had available a hand-drawn channel network map (field survey done by Joel Scheingross and Eric Winchell, University of California, Berkeley). The digitized version of the hand-drawn map is shown in Figure 3 as well. As can be seen, the part of the network close to the outlet is composed by *active* channels (channels with well defined banks and presence of bed material), while the part close to the divide consists of inactive (poorly formed channels with limited bed material but with definable channel banks) and *transient* channels (which present characteristics in between the inactive and active channels). Because the channel network of Skunk Creek is disrupted by deep-seated landsliding (see also analysis of *C. Gangodagamage et al.* (submitted manuscript, 2009)) and is discontinuous in its upper reaches, several channel heads occur along individual valley paths (see Figure 3). We preserve this discontinuity to explore how well we can detect not only channel initiation points but also channel disruptions through our proposed techniques. The channel network of the Skunk Creek is a very challenging basin for testing a channel extraction methodology. Nevertheless, the capability of our methodology in capturing channel disruptions, as shown in this section, makes it a very interesting application.

3.1. Preprocessing: Regularization of High-Resolution Digital Elevation Data Through Nonlinear Filtering

[21] We focus our analysis on a 200 m \times 200 m portion of the Skunk Creek, referred to as portion A (see Figure 4). The landscape A has been processed with a Gaussian filter (isotropic linear diffusion) and the Perona-Malik filter (anisotropic nonlinear diffusion). To allow comparison of the two filtered landscapes, the time of forward diffusion (iteration steps) has been set to 50 iterations in both (in general, there is no exact mathematical correspondence between the corresponding diffusion times). This corresponds to a Gaussian spatial filter of approximate $\sigma = 7$ m (scale of smoothing of the landscape of approximately $4\sigma = 28$ m) [see *Lashermes et al.*, 2007, Table 1]. As is apparent from the theory, no such unique and uniform equivalent spatial scale of smoothing can be assigned to the nonlinearly filtered landscape as the effective smoothing scale varies locally at every point depending on the local gradient. Specifically, the effective spatial scale of smoothing is smaller in the vicinity of feature boundaries (e.g., the channel boundaries, where the gradient is large and the edge stopping function of equation (8) assigns a small diffusivity coefficient), and larger in areas of spatially homogeneous and small gradients (recall also the example shown in Figures 1 and 2). The Perona-Malik filter used in this analysis is that of equation (8) with parameter λ estimated from the 90% quantile of the probability distribution function (pdf) of the gradients, as also suggested by *Perona and Malik* [1990] (the selection of such a parameter can be made fully automatic also following the robust statistics approach

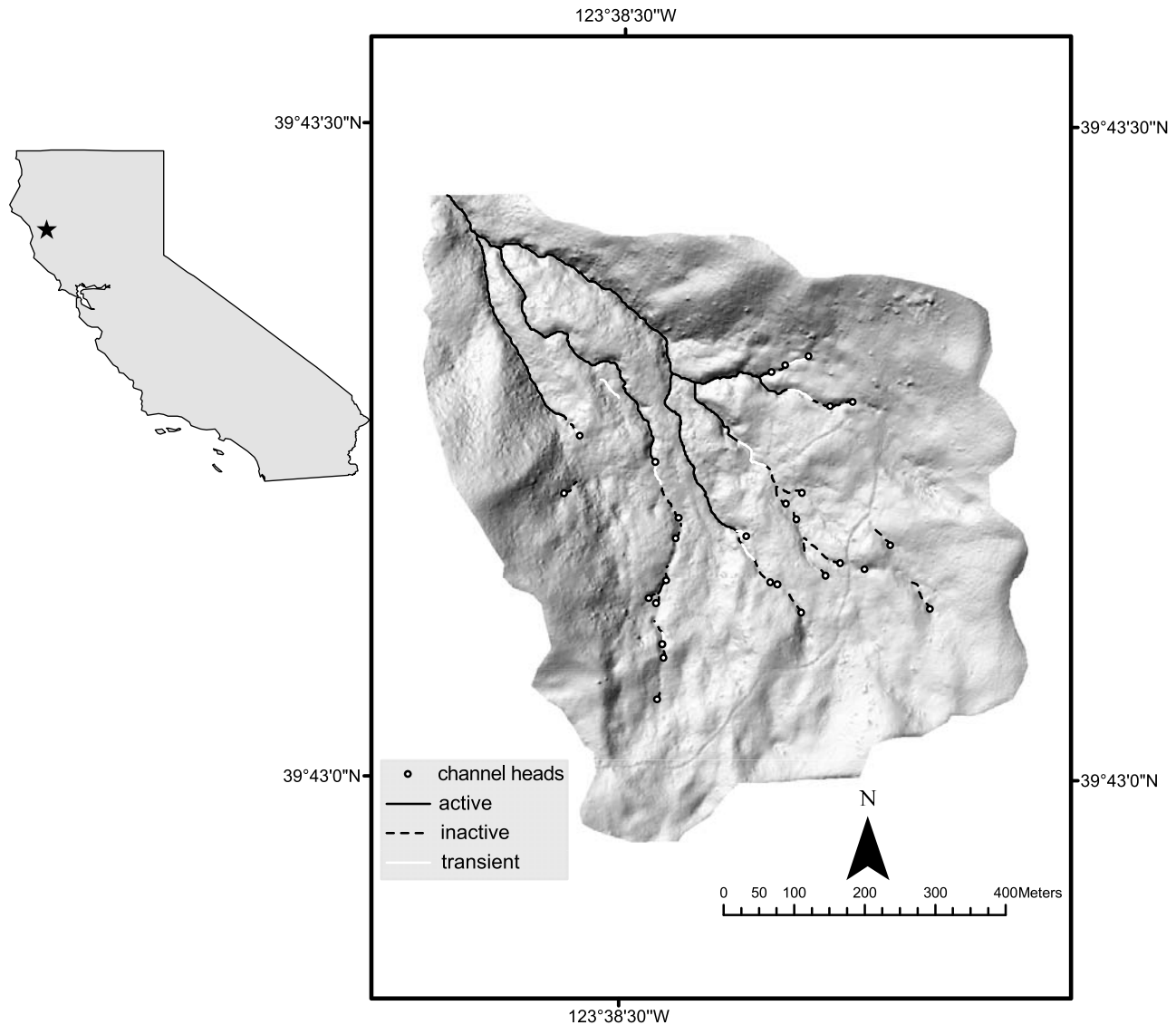


Figure 3. Skunk Creek, a 0.54 km² tributary located just upstream of Elder Creek, part of the South Fork Eel River in northern California. The upper half of the basin consists of active channels (well defined banks and presence of bed material), while the bottom half consists of inactive (poorly formed channels with limited bed material) and transient channels (with characteristics in between active and inactive).

by *Black et al.* [1998]). Note that the standard deviation of the Gaussian kernel and the number of iterations of the Perona-Malik filter have to be defined based on the scale of the objects we want to remove from the data. In particular the notion of 50 iterations has to be interpreted as a parameter of the algorithm. It represents the number of steps needed to achieve noise reduction and discontinuities enhancement before proceeding with the channel extraction.

[22] Figure 5a shows the original landscape at the resolution of 1 m with 3 m contours superimposed on it, as well as the computed gradients and curvatures (using simple first- and second-order numerical differentiation). Figures 5b and 5c show the filtered landscapes with the Gaussian filter and Perona-Malik filter, respectively, using for both 50 iterations as the stopping time of the forward diffusion as explained

above. The curvature reported here in all cases is the (geometric) curvature of the isoheight contours:

$$\kappa = \nabla \cdot (\nabla h / |\nabla h|) \quad (12)$$

computed by standard finite differences. The advantages in using the geometric curvature instead of the Laplacian will be addressed later in this section.

[23] Several observations can be made from Figure 5. First, it is easily seen from Figure 5b that the Gaussian filter smooths the contours along the channels much more than the Perona-Malik filter. This is expected from the theoretical properties of the Perona-Malik filter which deforms the landscape much less along the discontinuities. In fact, the Perona-Malik filter achieves a limited deformation of con-

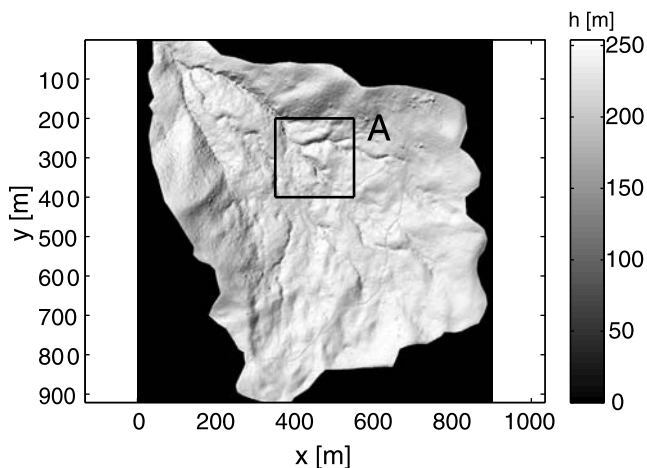


Figure 4. Location of the 200 m × 200 m square, named portion A, in Skunk Creek.

tours along the discontinuities such that it encourages the localization of these features. It is also observed that the areas of the landscape over which the curvature is positive (along the channelized areas) are much broader, and thereby deformed, in the Gaussian filtered landscape than in the Perona-Malik landscape. This is also expected from the basic properties of the two filters. One can argue that the Gaussian filtering (isotropic diffusion) could be stopped earlier, i.e. smaller spatial scale of filtering, to result in better localization of the channelized valleys. However, as it will be seen later, such a smaller-scale filtering would not adequately eliminate the isolated high curvature areas that are not pertinent to channel extraction. Furthermore, nonlinear diffusion is enhancing the discontinuities (acting in those regions as backward diffusion as shown by *Perona and Malik* [1990]; see also Appendix), which is critical for facilitating the automatic channel network extraction.

[24] Figure 6 shows the pdfs of the geometric curvatures of the original data and the filtered landscapes as well as the

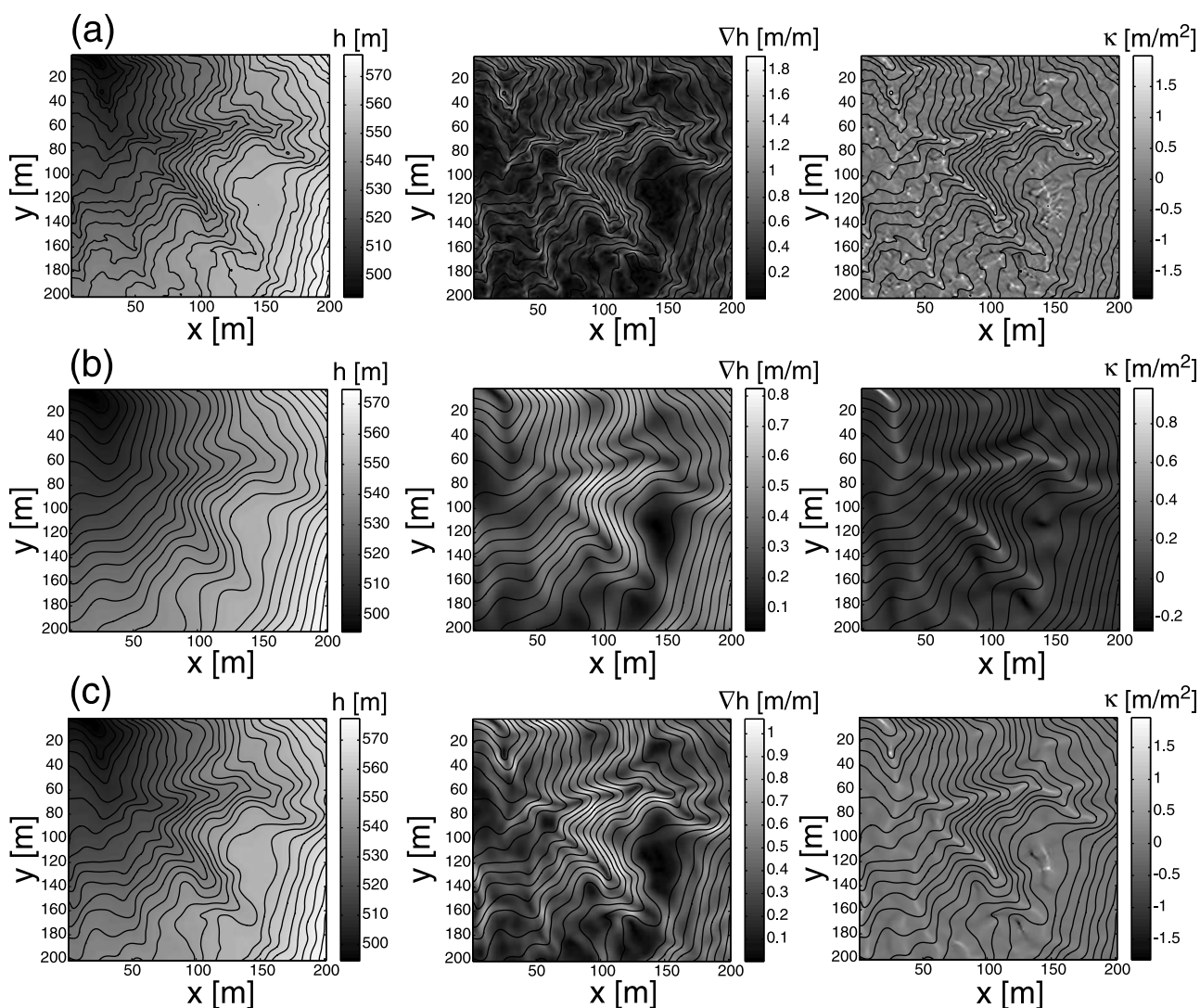


Figure 5. Comparison of the (left) elevation, (middle) gradient, and (right) curvature between the (a) original data, (b) Gaussian filtered data (scale $\sigma = 7$ m), and (c) Perona-Malik filtered data (50 iterations) computed in portion A of Skunk Creek shown in Figure 4. In all plots, elevation contours at 3 m spacing are superimposed. Notice the sharper localization of the channels in the Perona-Malik filtered lidar data.

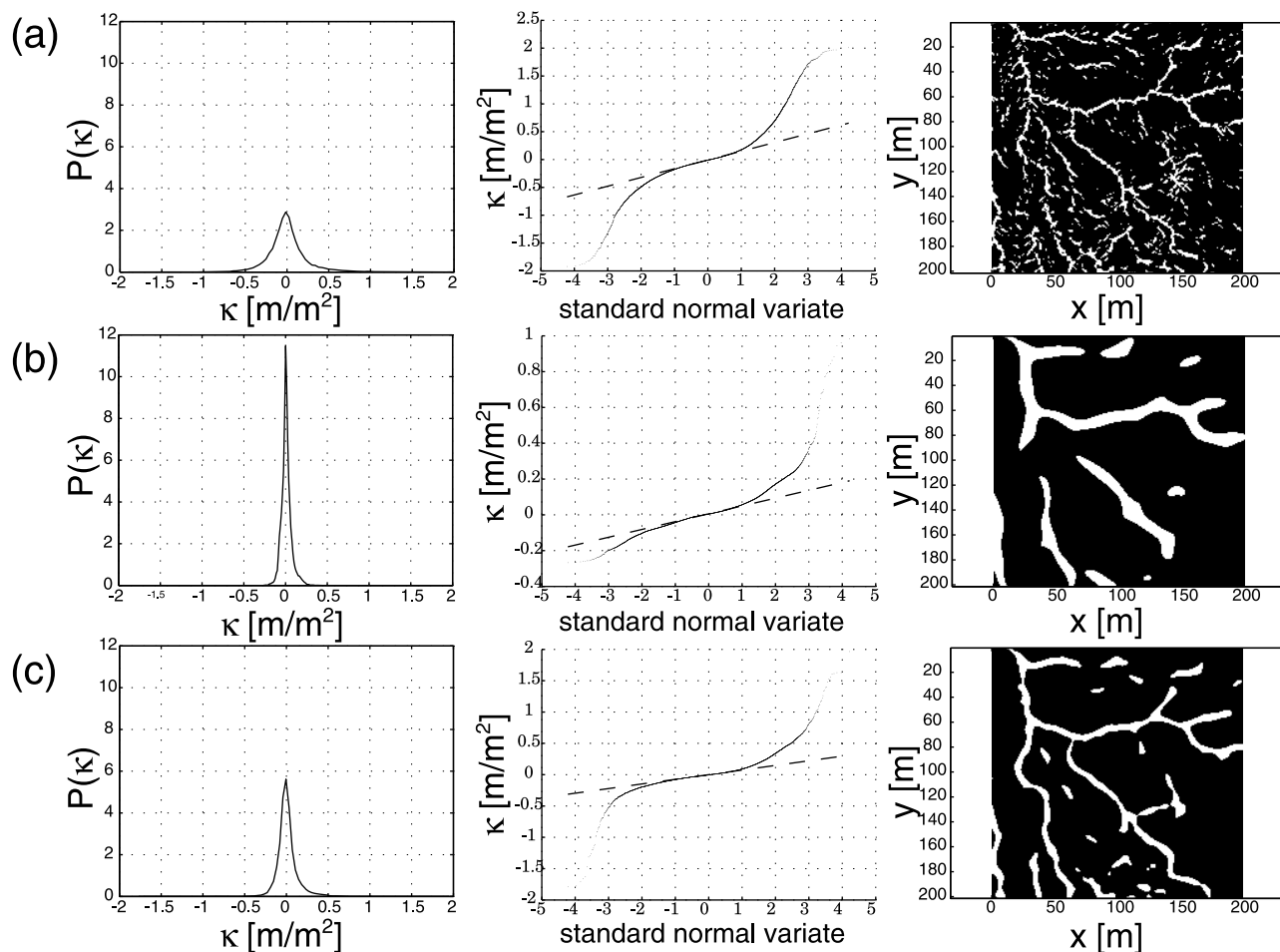


Figure 6. Comparison of the pdfs of (left) curvature, (middle) q-q plots of curvature from which the threshold value is determined, and (right) skeleton of pixels with above-threshold curvature for the (a) original data, (b) Gaussian filtered data (scale $\sigma = 7$ m), and (c) Perona-Malik filtered data (50 iterations) computed in portion A of Skunk Creek shown in Figure 4. The Perona-Malik filter does the best in terms of accurately localizing the channelized valleys while reducing background noise (see text for more discussion).

quantile-quantile plots of those curvatures. As discussed in the work of *Lashermes et al.* [2007] for the Laplacian, the sudden change in the statistical signature of the landscape, depicted by the (positive) curvature at which the pdf deviates from a Gaussian pdf, marks the transition from hillslopes to valleys. It is interesting to observe that although the actual value of the threshold curvature is different for the original image and the two filtered images, as expected, the quantile at which this transition occurs is scale- and filter-independent and as reported in the work of *Lashermes et al.* [2007] for the Laplacian, corresponds to the standard normal deviate of $z = 1$ (approximately the 84th quantile of the pdf of curvatures). Figure 6 (right) depicts the pixels at which the curvature was greater than the threshold curvature identified from the corresponding pdfs; white pixels correspond to pixels with curvature greater than the threshold value while black pixels correspond to pixels with curvature smaller than the threshold value. Several observations can be made. First, the above-threshold curvature pixels in the original high-resolution data depict the channelized part of the landscape but at the same

time one sees several isolated small areas which are strongly convergent due to the high frequency variability present on the landscape (e.g., bumpy ground, vegetation, etc.). The operation of smoothing is thus performed in order to focus the channel identification on the scale of interest. Second, the above-threshold curvature pixels on the Gaussian filtered landscape eliminate the noise and nicely depict the valleys or channelized areas only; however, the corridors of the convergent areas are too wide due to the smoothing of the landscape which has been done at the scale of approximately 28 m throughout the landscape.

[25] The above-threshold curvature pixels in the Perona-Malik filtered landscape (shown in Figure 6c), depict in a much sharper way the channelized valleys. Of course, a smaller-scale Gaussian filter would also result in a sharper delineation of the channelized valleys. While this is true, however, the smaller scale of smoothing would not eliminate the isolated small convergent areas which are not part of the channel network. This is demonstrated in Figure 7, which displays the above-threshold curvature pixels for three standard deviations of the Gaussian filter: $\sigma = 2$ m

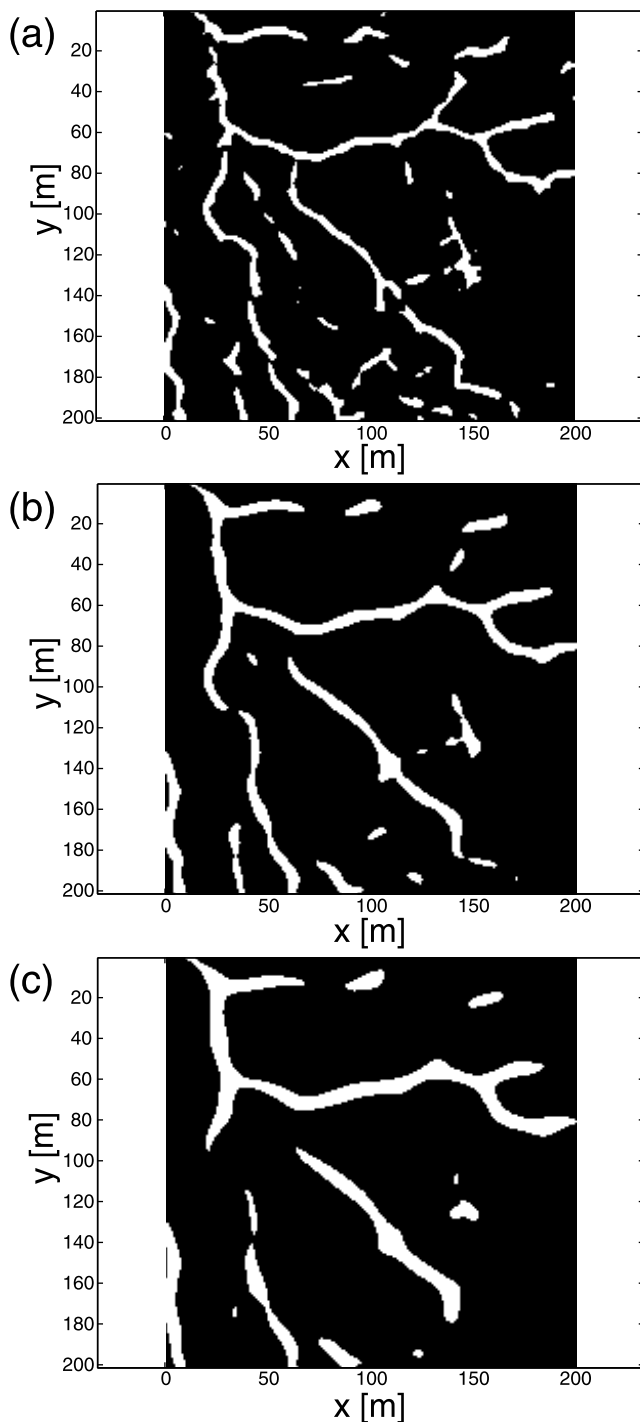


Figure 7. Comparison of the images obtained thresholding the curvature computed on the Gaussian filtered data with $\sigma = 2$ m, 4 m, 6 m (landscape smoothing scales of 8.9 m, 17.8 m, and 26.7 m, respectively). White pixels indicate pixels with above-threshold curvature. The plots refer to portion A of Skunk Creek shown in Figure 4.

(landscape smoothing scale $a = 8.9$ m); $\sigma = 4$ m (landscape smoothing scale $a = 17.8$ m); $\sigma = 6$ m (landscape smoothing scale $a = 26.7$ m). It is noted by comparing Figures 6c and 7 that the Perona-Malik localization of the channelized valleys (measured by the width of the white corridors) is

comparable to the localization provided by the Gaussian filter at scale of approximately 9 m ($\sigma = 2$ m). However, at this small scale of smoothing, the Gaussian filtering results in many more isolated high curvature areas as can be seen in Figure 7a compared to Figure 6c. Thus we conclude overall, that the Perona-Malik filter is a more efficient filter to use for preprocessing of the raw data (to produce what is called “regularized data”) on which further operations for automatic channel extraction can be performed.

[26] It is also worth pointing out the advantage of using the (geometric) curvature κ instead of the Laplacian. This can be seen by comparing Figure 6b to Figure 8. The figures show the skeletons of pixels above-threshold curvature obtained on the Gaussian filtered data (scale $\sigma = 7$ m) using geometric curvature (Figure 6b) and Laplacian (Figure 8). Note how sharper and well defined is the skeleton obtained using the geometric curvature.

[27] Before demonstrating in the next section the geodesic energy minimization approach for the automatic extraction of the whole channel network of the Skunk Creek, we note that one can further process the regularized data to eliminate even more the occasional isolated convergent pixels seen in Figure 6c. This is a further operation which can be easily done via a contributing area threshold, where the threshold used has to be small enough not to interfere with channel initiation. For example, Figure 9 shows the skeleton of Figure 6c after applying the additional contributing area threshold of $A = 3000$ m², meaning that only the pixels with contributing area equal to or above this threshold were selected. The contributing area was computed using the Dinf algorithm [Tarboton, 1997]. We have then compared this value to the minimum contributing area at the channel heads, obtained using the same algorithm at the 11 farthest surveyed channel heads in Skunk Creek. As it can be seen from the histogram of the contributing area shown in Figure 10, the minimum value is equal to 3329 m², thus the chosen contributing area threshold of 3000 m² does not interfere with channel initiation. It is noted that, while the curvature threshold is easily identifiable from the

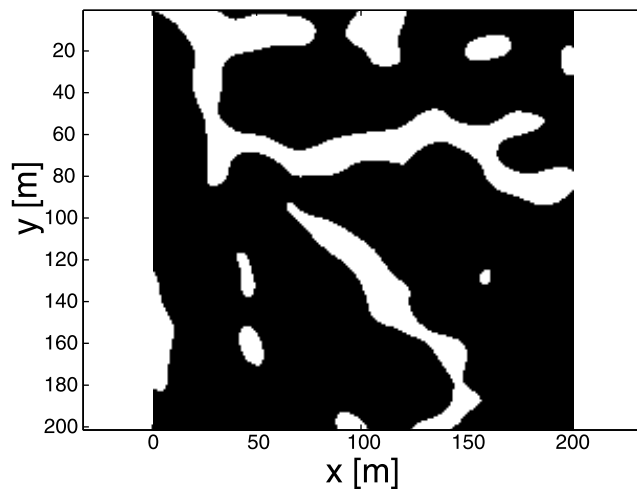


Figure 8. Skeleton of pixels above threshold curvature for the Gaussian filtered data using the Laplacian with $\sigma = 7$ m (landscape smoothing scale of 31.1 m). The plot refers to portion A of Skunk Creek shown in Figure 4.

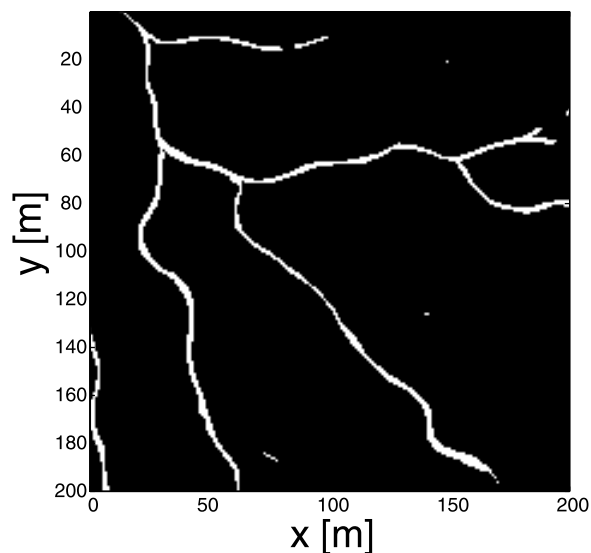


Figure 9. Skeleton obtained by thresholding curvature and contributing area for the portion A of Skunk Creek shown in Figure 4. Introducing the contributing area criterion eliminates all the isolated pixels which have a positive curvature above threshold but are not part of the channel network.

quantile-quantile plot, as explained earlier, the contributing area threshold is an arbitrarily chosen value, the smallest able to reduce the noise further in the skeleton of likely channelized pixels. It is observed that this further operation not only removes isolated convergent areas, but also further narrows the width of the likely channelized valleys providing a better preprocessed data on which channel heads are identified for the geodesic optimization to be performed (see discussion later in the application to the Skunk Creek basin).

3.2. Automatic Extraction of Channel Paths From the Regularized Data

[28] In this section we focus on the regularized data set of Skunk Creek obtained through nonlinear filtering and illustrate how the concepts of geodesics and energy minimization described earlier allow a fast and efficient extraction of the channel network. The first step of the extraction procedure is the creation of the skeleton obtained by nonlinear filtering and thresholding the curvature and the contributing area, as discussed in the previous section. The threshold curvature was easily identified by a clear change in the statistical behavior of the curvature, while the threshold area was set to a value of 3000 m^2 . The extracted skeleton for the Skunk Creek river basin is shown in Figure 11.

[29] Several observations can be made by comparing Figure 11 with the surveyed network shown in Figure 3. First, in Figure 3 one observes that most of the channels in the part of the network close to the divide are labeled as “transient” or “inactive” and indeed the extracted skeleton depicts this topography by a series of interrupted areas of high curvature (and large contributing area). Second, at the points where the surveyed channel heads are located, our algorithm depicts a substantial interruption in the channel-

ized valley. It is observed therefore, that the preprocessing already allows one to investigate more closely the richness of the landscape form, something not possible with other current algorithms.

[30] From the skeleton of Figure 11, we can detect the river network outlet, as the point with the maximum flow accumulation area, computed, for example, using the Dinf algorithm [Tarboton, 1997]. After the outlet of the network has been identified, we can proceed with the detection of the end points. First the algorithm uses the skeleton of Figure 11 to compute how many continuous elements compose the skeleton and how many pixels belong to each of them. With this we mean that we label with a sequential number all the parts of the skeleton which are completely connected and do not present disruptions (i.e., the skeleton is continuously equal to 1, while the disruption is represented by one or more pixels equal to zero). We call the variable representing the number of pixels in each connected element N and plot in Figure 12a its histogram. As it can be seen, the Skunk Creek skeleton is composed by 56 connected elements, one of which is composed by 4508 pixels and 55 much smaller elements. This is something we could have expected having already observed that Skunk Creek is an extremely disrupted basin, and we can deduce that the element composed by 4508 pixels is the one which includes the part of the basin close to the outlet (the most continuous one), while the 55 smallest elements compose the skeleton of the part of the basin close to the divide (which, as we already pointed out, appears extremely disrupted in agreement with the fact that the channels here are either inactive or transient). Note that some of these elements may also represent small isolated noisy areas still present in the data.

[31] Now that the connected elements of the skeleton are identified, the algorithm looks for the end points. These are identified as the points at which the branches end. Since the branches are wider than one pixel, the actual point taken as end point is the one which belongs to the minimum geodesic distance path. Thus we need to define the cost

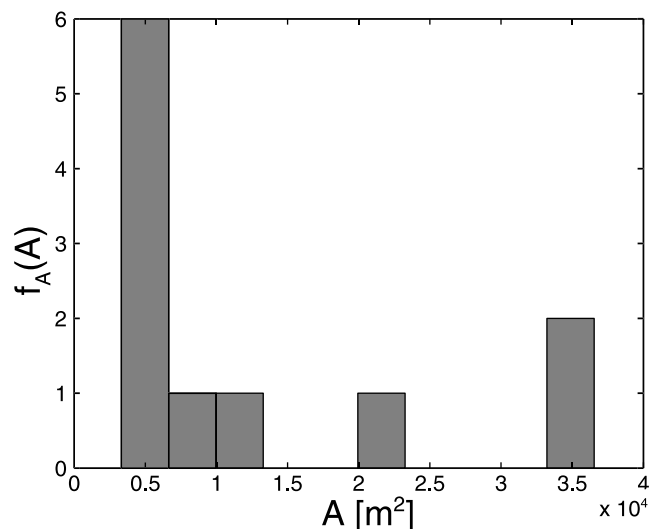


Figure 10. Histogram of the contributing area computed with the Dinf algorithm at the 11 farthest channel heads surveyed in Skunk Creek.

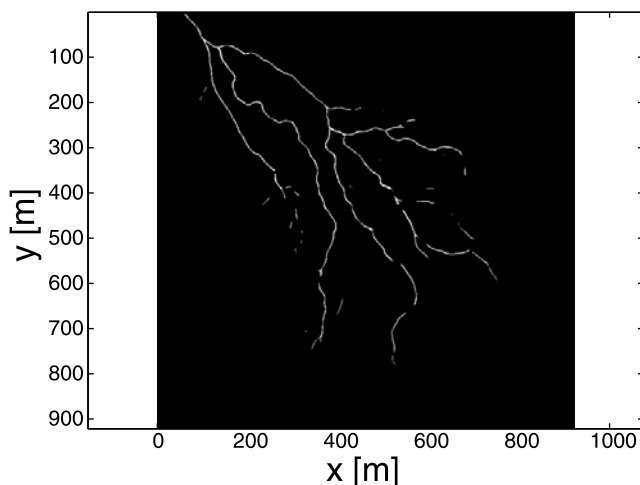


Figure 11. Skeleton obtained by thresholding curvature and contributing area for Skunk Creek.

function which will be used to identify the end points and connect them to the outlet through geodesic curves. This *cost function* was chosen to give penalty for selecting paths along which the drainage area does not have large flow accumulation and along which the curvature is not large compared to the surrounding points. The chosen form of the cost function ψ used in (10) is the following:

$$\psi = \frac{1}{(\alpha \cdot A + \delta \cdot \kappa)} \quad (13)$$

where A is the contributing area, κ is the curvature (of isoheight contours for our examples), and α and δ are constants which have to be chosen appropriately for the application at hand. The purpose of these constants is to take care of the dimensionality of ψ (as A is measured in m^2 , while κ in $1/\text{m}$) and of the difference in the order of magnitude between the quantities employed (A varies between 1 and $5 \times 10^5 \text{ m}^2$, while κ has been normalized and thus varies between 0 and 1).

[32] We will discuss later in this section how the choice of the constants α and δ can be made. For now, to illustrate how the end points are detected, let us assume we have identified the optimal parameters of the cost function (13) for our application, namely $\alpha = 1 \text{ m}^{-2}$ and $\delta = 10^3 \text{ m}$ (see discussion later in this section on how these parameters can be determined). We focus on the $200 \text{ m} \times 200 \text{ m}$ portion A of the Skunk Creek used in section 3.1. Figure 13a shows the skeleton of Skunk Creek (the same previously shown in Figure 9) and Figure 13b shows the end points as detected by the algorithm and indicated by a white circle. We can notice that the locations marked as A, B, and C do not appear to belong to a channel, but rather to be small convergent areas still present in the skeleton after preprocessing. It is clear that we need to identify these elements and ignore them, such that they will not be erroneously considered as channels. If we plot again the histogram of N , the number of pixels belonging to each connected element of the skeleton, ignoring the largest element, as shown in Figure 12b, we notice that there is a large number of

small connected elements located below and around a value of $N = 10$ pixels. We can interpret these elements as small isolated convergent areas and detect the end points only on the elements of the skeleton with $N > 10$ pixels. Note that we expect the identification of this threshold of N to be much simpler in the case of a basin more homogeneous than Skunk Creek. Due to the nature of the basin here in analysis, the choice of this value of N is extremely challenging, while a more homogeneous basin would probably present the skeleton as a unique connected element, with a few smaller ones, which could be easily interpreted as isolated areas. The result of adding a threshold $N > 10$ pixels in the end points detection can be seen in Figure 13c. Locations A, B, and C are now ignored and the end points (indicated by white circles) are identified only on the branches that appear to be channels. Following this procedure we have identified

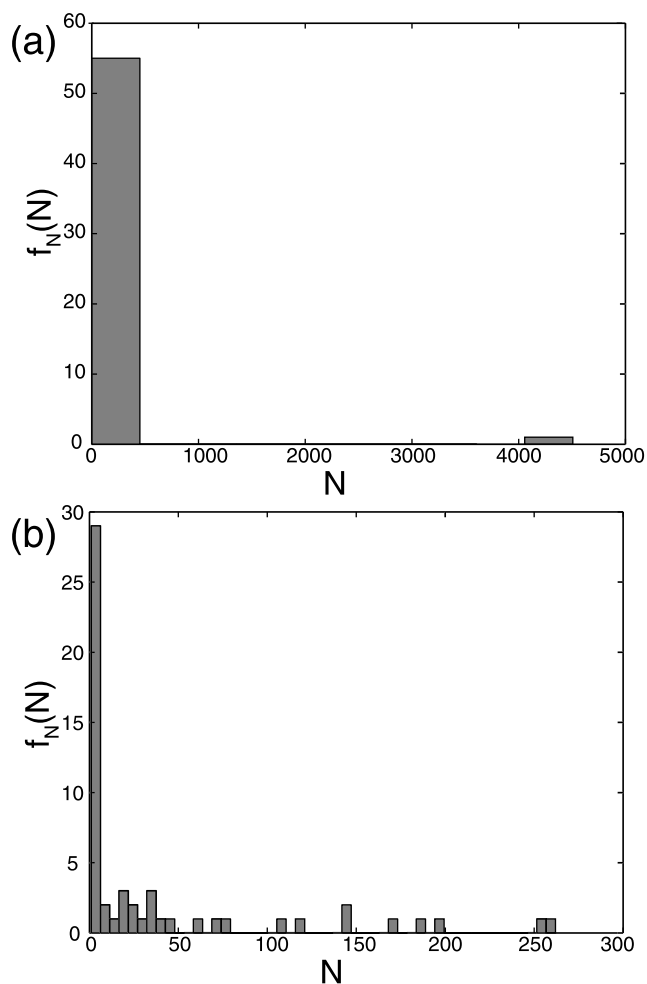


Figure 12. (a) Histogram of the number of pixels belonging to each connected element of the skeleton of Skunk Creek. The skeleton is composed by 56 elements of which one includes the majority of the pixels. (b) Excluding the most connected element, the histogram highlights a large number of small connected elements below and around $N = 10$ pixels. This value can be interpreted as the size of small isolated convergent areas which do not belong to channels.

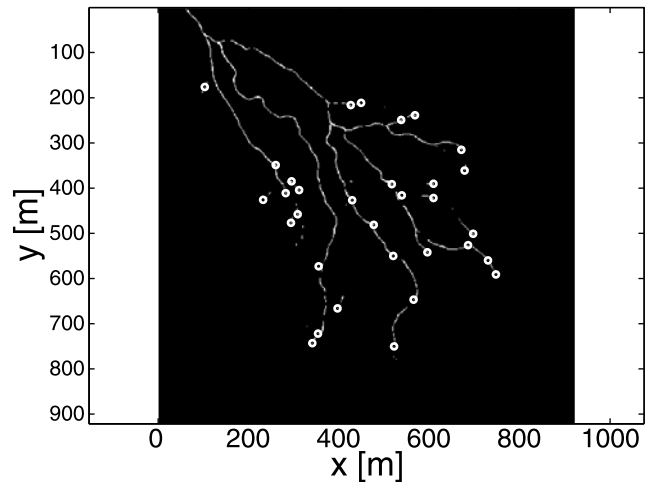
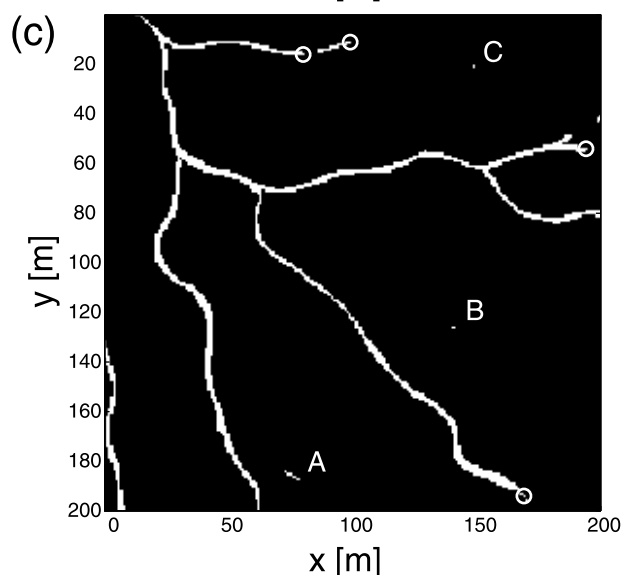
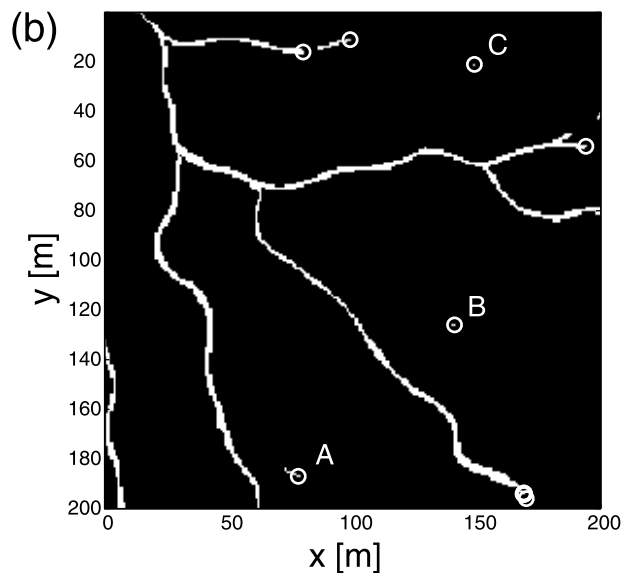
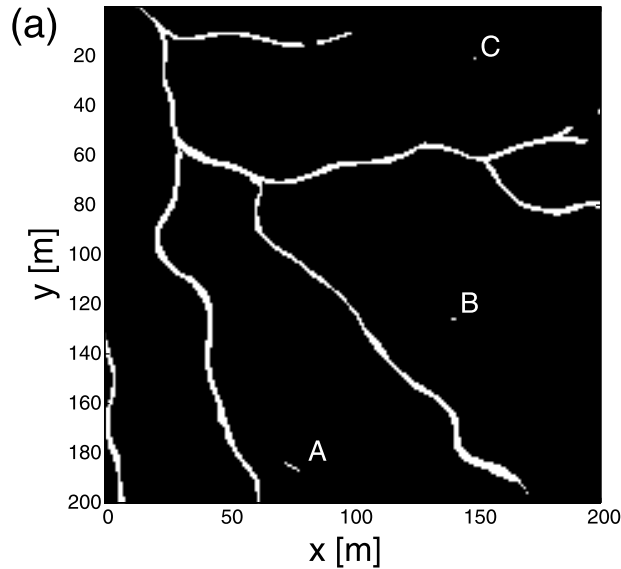


Figure 14. End points automatically detected in Skunk Creek.

all the end points in the Skunk Creek skeleton, as shown in Figure 14.

[33] After all the end points have been detected, we connect them with geodesic curves through the above defined cost function (13). Let us now discuss the selection of the constants α and δ . A helpful quantity in the definition of the constants α and δ is the geodesic distance d (11). Since the geodesic curves (10) are computed by gradient descent on d , then d can be used to understand how optimal is the choice of the constants. This is illustrated in Figure 15. Figures 15a–15j show the geodesic distances d and the extracted network correspondent to different choices of α and δ in the cost function ψ (13). Figures 15a and 15c show the geodesic distances d corresponding to $\alpha = 1 \text{ m}^{-2}$ and $\delta = 0 \text{ m}$ and $\alpha = 0 \text{ m}^{-2}$ and $\delta = 1 \text{ m}$ respectively, and Figures 15b and 15d the corresponding extracted networks. It is clear that using only one of the two quantities does not give good results. Figures 15e through 15j show the geodesic distances and the extracted networks for $\alpha = 1 \text{ m}^{-2}$ and $\delta = 1, 10^3, 10^5 \text{ m}$. It can be seen how the choice of $\alpha = 1 \text{ m}^{-2}$ and $\delta = 1000 \text{ m}$ gives the smallest values of the geodesic distance along the skeleton of the network. This can be used as guidance to ensure an optimal computation of the geodesic curves. Note that the value of $\delta = 1000 \text{ m}$ corresponds to the order of magnitude of the mean contributing area computed on the whole surface $\bar{A} \simeq 550 \text{ m}^2$.

[34] Figure 16 shows the extracted channel network obtained for the Skunk Creek with $\alpha = 1 \text{ m}^{-2}$ and $\delta = 1000 \text{ m}$ and compared to the surveyed data. As discussed before, this is a challenging basin for the automatic channel network extraction due to many interruptions due to land-

Figure 13. Detection of the end points. (a) Skeleton-obtained thresholding curvature and contributing area in portion A of Skunk Creek. (b) Without a threshold in N , the number of pixels composing each connected element, locations A and B are identified as channels. (c) The threshold $N > 10$ pixels allows to exclude locations A and B from the end points detection. End points are here indicated by a white circle.

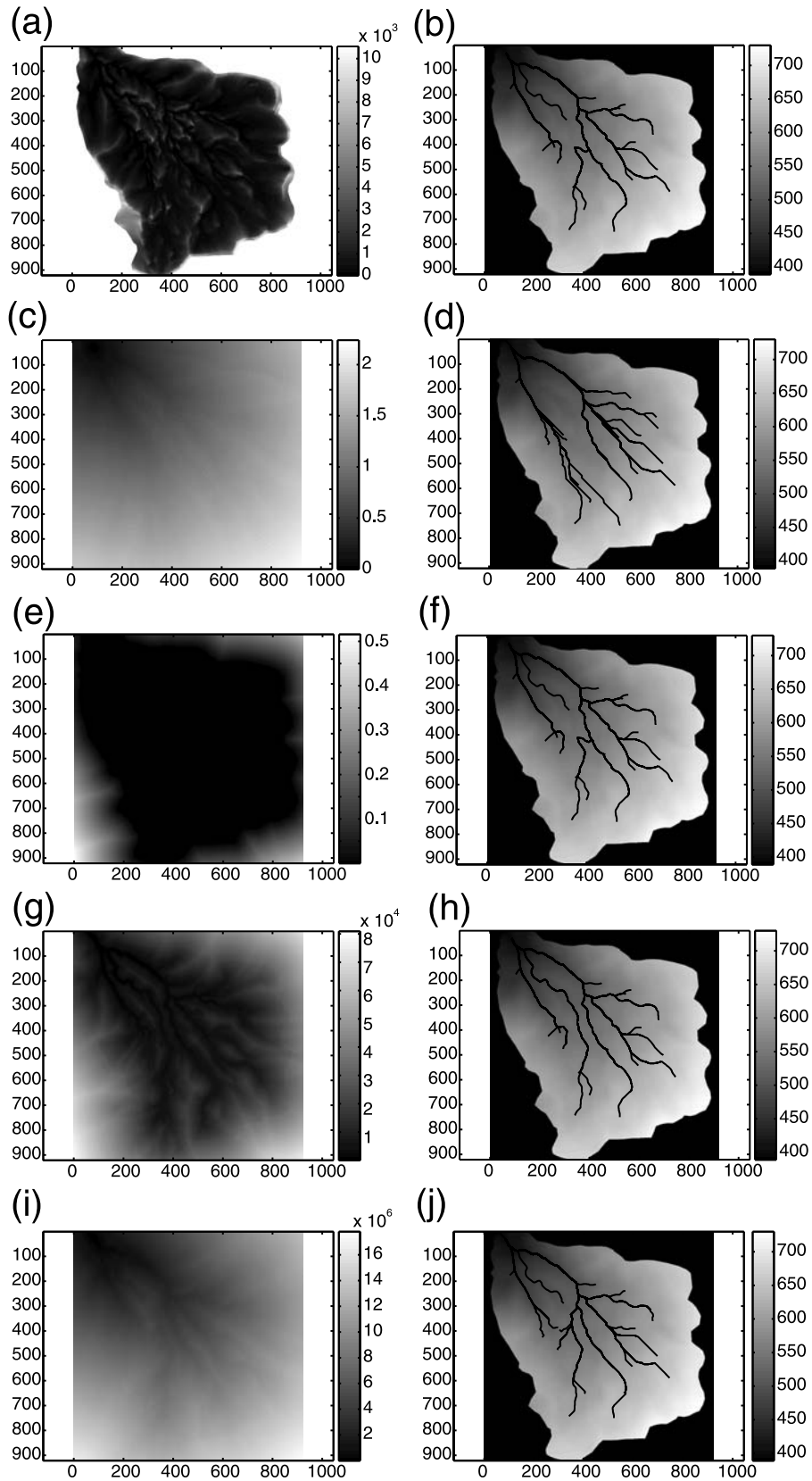


Figure 15. The geodesic distances d and the extracted networks for different choices of the parameters of the cost function ψ . The geodesic distances are useful in understanding if the choice of the cost function guarantees the optimal tracing of geodesic curves. (a and b) $\psi = \frac{1}{A}$; (c and d) $\psi = \frac{1}{\kappa}$; (e and f) $\psi = \frac{1}{A+\kappa}$; (g and h) $\psi = \frac{1}{A+10^3 \cdot \kappa^2}$; (i and j) $\psi = \frac{1}{A+10^5 \cdot \kappa}$.

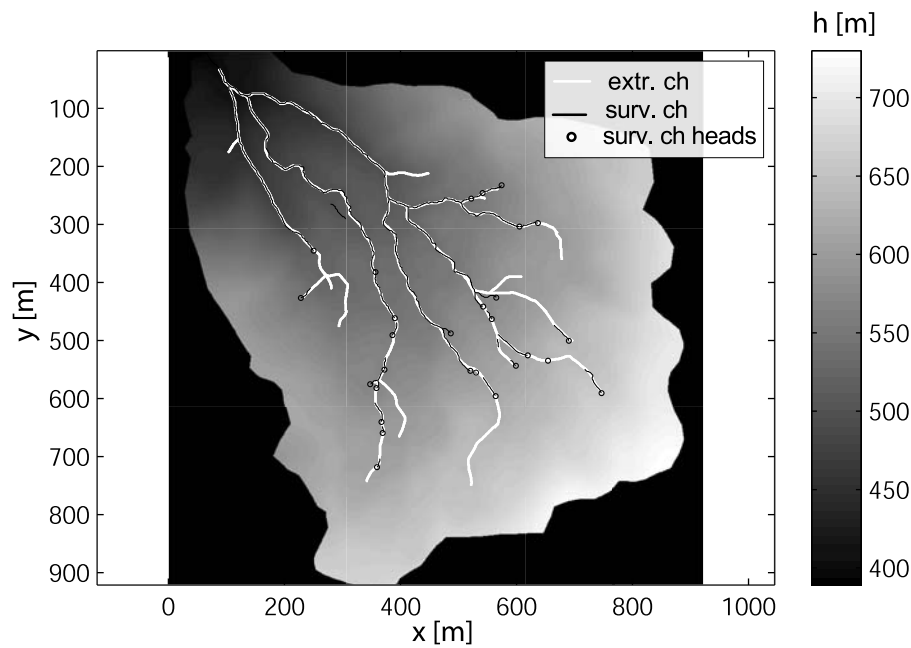


Figure 16. Automatically extracted river network for Skunk Creek using the geodesic optimization on the Perona-Malik filtered landscape compared to the digitized surveyed data.

slides and debris flows. Nevertheless, the automatically extracted channel network compares well with the field-surveyed river network. Recall that the only information that was externally provided was the threshold area of 3000 m^2 and the values of the parameters α and δ , though guidelines for the possible automatic selection of these parameters were provided as well.

[35] As discussed earlier, our algorithm allows the detection of channel disruptions (see Figure 11) which are depicted in the skeleton and can be kept before the geodesic optimization is performed. The channels are traced continuously to the farthest end points detected, but the user knows the location and the extent of the disruptions from the skeleton. Figures 17a and 17b show the histogram of the length of the channel disruptions measured on the surveyed data of Figure 3 and on the extracted skeleton of Figure 11. As it can be seen the extracted network of Skunk Creek shows, statistically, the same level of disruptiveness characteristic of the area.

4. Concluding Remarks

[36] High-resolution DEMs offer new opportunities for extracting detailed features from landscapes (e.g., channels, disruptions, channel heads), but also challenges in developing extraction methodologies that are objective and computationally efficient. The problem really becomes one of image processing relying on scale-space representation, i.e., coarsening the landscape without smoothing out features of interest and detecting features efficiently. In this paper we introduced a geometric framework for the extraction of channel networks from lidar data. The proposed approach includes two main components: the preprocessing of the data via nonlinear diffusion, to reduce noise and enhance features that are relevant to the network extraction,

and the computation of channel networks in the filtered data via geodesic curves that incorporate geomorphological knowledge such as contributing area and (geometric) curvature. The methodology presented in this paper has been applied to Skunk Creek, a tributary of the South Fork Eel River basin in northern California. Despite the challenges presented by the basin analyzed, which is a complex landslide-disrupted basin, the proposed methodology has demonstrated to be computationally efficient and able to detect, not only channels, but also the presence of channel disruptions.

[37] This work, which introduces the idea of approaching geomorphological analysis as a geometric task, opens the door to many problems in the automatic extraction of information from lidar data. For the particular case of channel networks, it is important to study the possible benefits of using other nonlinear equations for preprocessing and the introduction of additional features in the geodesic penalty function. Similarly, the exploitation for geomorphological analysis of other models which are popular in the partial differential equations and variational formulations in image processing community, such as the Mumford-Shah functional [Mumford and Shah, 1989], is of great interest. For example, the channel networks can be considered as discontinuity fields and outliers, and as such be automatically computed by such an approach [Sapiro, 2001]. Beyond this, the methodology is being presented here for the case of a tributary system, but with an appropriate modification of the cost function, could be applied to a distributary or mixed systems. Moreover channel networks are just one of the many important features in landscapes, and the exploration of the geometric approach here initiated for the extraction of other geomorphic features, such as landslides, debris flow regions,

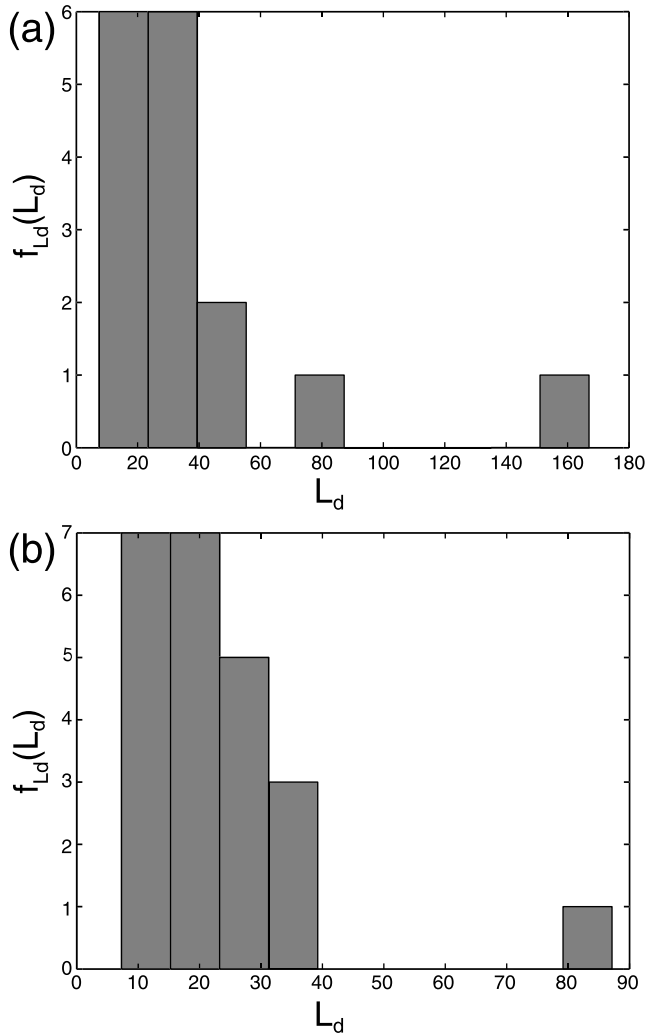


Figure 17. (a) Histogram of the length of the channel disruptions L_d measured on the surveyed data. (b) Histogram of the length of the channel disruptions L_d measured on the extracted data.

ravines, channel morphology, etc., is a subject of future research.

Appendix A

[38] In this Appendix we illustrate the property of the Perona-Malik filtering. In particular we include part of the formulation in the original *Perona and Malik* [1990] paper to show that this filter acts as a backward diffusion in regions of high gradients such that it results in enhancing these edges for easy extraction. We illustrate this via a simple 1-D example of an *edge* modeled as a step function convolved with a Gaussian, assumed to be aligned with the y axis (see Figure A1). The divergence operator in this case simplifies as follows:

$$\nabla \cdot [c(x, y, t) \nabla h] = \partial_x [c(x, y, t) \partial_x h] \quad (\text{A1})$$

Choose c to be a function of the gradient of h : $c(x, y, t) = p[\partial_x h(x, y, t)]$ and define the flux: $\phi(\partial_x h) \equiv c \cdot \partial_x h \equiv p(h_x) \cdot h_x$.

Then, the 1-D version of the nonlinear diffusion equation (7) becomes:

$$\partial_t h = \partial_x \phi(h_x) = \phi'(h_x) \cdot h_{xx} \quad (\text{A2})$$

We are interested in the variation in time of the slope of the edge, which is given by $\partial_t(h_x)$. If $c(\cdot) > 0$ and the function h is smooth, the order of differentiation may be inverted:

$$\partial_t(h_x) = \partial_x(h_t) = \partial_x[\partial_x \phi(h_x)] = \phi'' \cdot h_{xxx}^2 + \phi' \cdot h_{xxx} \quad (\text{A3})$$

Assuming the edge to be oriented such that $h_x > 0$, then, at the point of inflection, being the point with maximum slope, $h_{xx} = 0$, and $h_{xxx} \gg 0$. Then as can be seen from (A3) if $\phi'(h_x) > 0$ the slope of the edge decreases with time, while if $\phi'(h_x) < 0$ the slope increases with time (the edge becomes sharper with time). Several possible choices

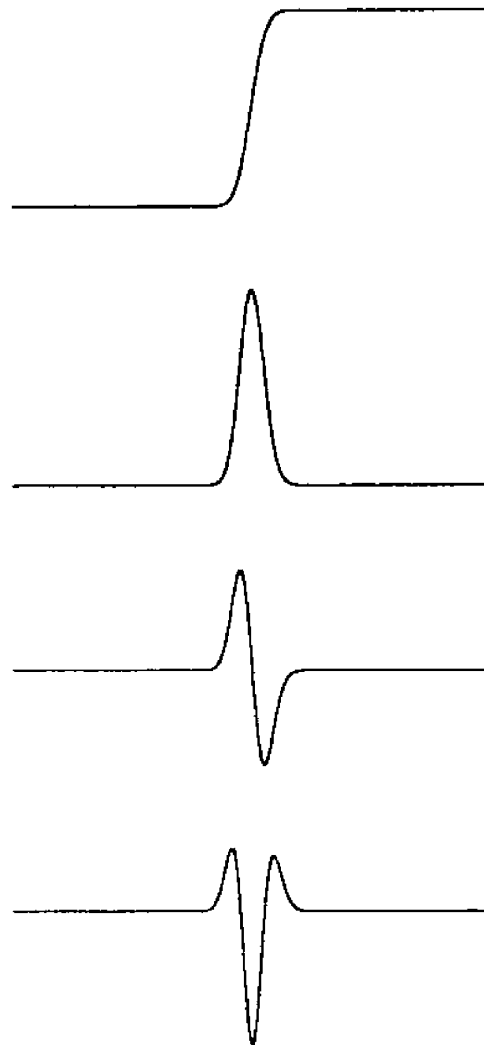


Figure A1. The 1-D edge modeled as a step function convolved with a Gaussian kernel and its first, second, and third derivatives. Figure adapted from *Perona and Malik* [1990] (copyright 1990 with permission from IEEE).

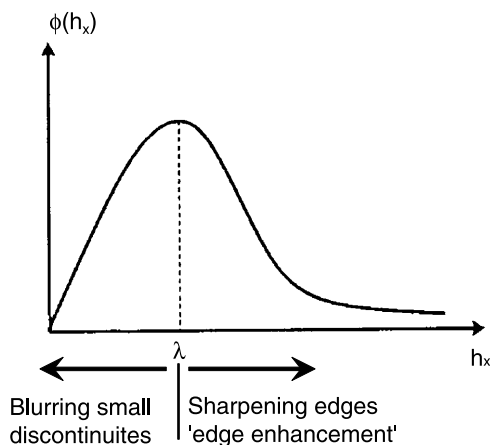


Figure A2. One form of the flux ϕ . There is a certain threshold value below which $\phi(\cdot)$ is monotonically increasing and beyond which $\phi(\cdot)$ is monotonically decreasing, achieving noise reduction and edge enhancement. Figure adapted from *Perona and Malik* [1990] (copyright 1990 with permission from IEEE).

of the function $\phi(\cdot)$ exist, one being the following (see Figure A2):

$$\phi(h_x) = C / \left(1 + (h_x/\lambda)^{1+\alpha} \right) \quad (\text{A4})$$

with $\alpha > 0$. This means that there is a certain threshold value related to λ and α , below which $\phi(\cdot)$ is monotonically increasing, and beyond which $\phi(\cdot)$ is monotonically decreasing, achieving noise reduction and edge enhancement. In a neighborhood of the steepest region of an edge, $\phi'(h_x)$ is negative, which means that the nonlinear diffusion acts as backward in time, thus achieving edge enhancement, while preserving the advantages of the stability given by the maximum principle satisfied by this type of elliptic equation. For more details the reader is referred to the original publication of *Perona and Malik* [1990].

[39] **Acknowledgments.** We thank Jean-Michel Morel for suggesting to incorporate the contributing area flow in the geodesic penalty function, which turned out to be critical in order to achieve the high-quality results here reported. We also thank him for initiating the visit of his student T. Do Trung to the University of Minnesota to collaborate in this project. This work has been supported by NSF (CDI grant EAR-0835789 and CMG grants EAR-082484 and EAR-0934871) as well as by the National Center for Earth surface Dynamics (NCED), a Science and Technology Center funded by NSF under agreement EAR-0120914. Other support to G. S. by NSF, ONR, NGA, DARPA, and ARO is acknowledged gratefully. Computer resources were provided by the Minnesota Supercomputing Institute, Digital Technology Center, at the University of Minnesota. Joel Scheingross and Eric Winchell are thanked for providing a difficult to make channel map of Skunk Creek. We thank David Olsen for his expert help with the manuscript preparation. Finally, the anonymous reviewers provided extremely useful feedback that helped to significantly improve the manuscript.

References

Almansa, A., F. Cao, and B. Rouge (2002), Interpolation of digital elevation models via partial differential equations, *IEEE Trans. Geosci. Remote Sens.*, 40(2), 314–325.
 Alvarez, L., P. L. Lions, and J. M. Morel (1992), Image selective smoothing and edge detection by nonlinear diffusion, *SIAM J. Numer. Anal.*, 29(3), 845–866.

Anderson, R. S. (1994), Evolution of the Santa Cruz Mountains, California, through tectonic growth and geomorphic decay, *J. Geophys. Res.*, 99(20), 161–179.
 Anderson, R. S., and N. F. Humphrey (1989), Interaction of weathering and transport processes in the evolution of arid landscapes, in *Quantitative Dynamic Stratigraphy*, edited by T. A. Cross, pp. 349–361, Prentice-Hall, Englewood Cliffs, N. J.
 Andrews, D. J., and R. C. Buckman (1987), Fitting degradation of shoreline scarps by a nonlinear diffusion model, *J. Geophys. Res.*, 92(12), 857–867.
 Ardizzone, F., M. Cardinali, M. Galli, F. Guzzetti, and P. Reichenbach (2007), Identification and mapping of recent rainfall-induced landslides using elevation data collected by airborne lidar, *Nat. Hazards Earth Syst. Sci.*, 7(6), 637–650.
 Band, L. E. (1986), Topographic partition of watersheds with digital elevation models, *Water Resour. Res.*, 22(1), 15–24.
 Black, M., G. Sapiro, D. Marimont, and D. Heeger (1998), Robust anisotropic diffusion, *IEEE Trans. Image Process.*, 7(3), 421–432.
 Braunmandl, A., T. Canarius, and H. P. Helfrich (2003), Diffusion methods for form generalisation, in *Dynamics of Multiscale Earth Systems, Lect. Notes Earth Sci.*, vol. 97, edited by H. J. Neugebauer and C. Simmer, pp. 89–101, Springer, Berlin.
 Burt, P., and E. Adelson (1983), The Laplacian pyramid as a compact image code, *IEEE Trans. Commun.*, COM-31, 532–540.
 Catté, F., P.-L. Lions, J.-M. Morel, and T. Coll (1992), Image selective smoothing and edge detection by nonlinear diffusion, *SIAM J. Numer. Anal.*, 29(1), 182–193.
 Cavalli, M., and L. Marchi (2008), Characterisation of the surface morphology of an alpine alluvial fan using airborne lidar, *Nat. Hazards Earth Syst. Sci.*, 8(2), 323–333.
 Cavalli, M., P. Tarolli, L. Marchi, and G. Dalla Fontana (2008), The effectiveness of airborne lidar data in the recognition of channel bed morphology, *Catena*, 73, 249–260, doi:10.1016/j.catena.2007.11.001.
 Costa-Cabral, M. C., and S. J. Burges (1994), Digital elevation model networks (DEMON): A model of flow over hillslopes for computation of contributing and dispersal areas, *Water Resour. Res.*, 30(6), 1681–1692.
 Dial, R. B. (1969), Algorithm 360: Shortest-path forest with topological ordering, *Commun. ACM*, 12(11), 632–633.
 Dietrich, W. E., C. J. Wilson, D. R. Montgomery, and J. McKean (1993), Analysis of erosion thresholds, channel networks and landscape morphology using a digital terrain model, *J. Geol.*, 101(2), 259–278.
 Dietrich, W. E., D. Bellugi, and R. Real de Asua (2001), Validation of the shallow landslide model, SHALSTAB, for forest management, in *Land Use and Watersheds: Human Influence on Hydrology and Geomorphology in Urban and Forest Areas, Water Sci. Appl. Ser.*, vol. 2, edited by M. S. Wigmosta and S. J. Burges, pp. 195–227, AGU, Washington, D. C.
 Dijkstra, E. (1959), A note on two problems in connection with graphs, *Numer. Math.*, 1(1), 269–271.
 Do Carmo, M. P. (1976), *Differential Geometry of Curves and Surfaces*, Prentice-Hall, Englewood Cliffs, N. J.
 Frankel, K. L., and J. F. Dolan (2007), Characterizing arid region alluvial fan surface roughness with airborne laser swath mapping digital topographic data, *J. Geophys. Res.*, 112, F02025, doi:10.1029/2006JF000644.
 Giannoni, F., G. Roth, and R. Rudari (2005), A procedure for drainage network identification from geomorphology and its application to the prediction of the hydrologic response, *Adv. Water Resour.*, 28(6), 567–581.
 Glenn, N. F., D. R. Streutker, D. J. Chadwick, G. D. Tahckray, and S. J. Dorsch (2006), Analysis of lidar-derived topography information for characterizing and differentiating landslide morphology and activity, *Geomorphology*, 73, 131–148.
 Hancock, G. R., and K. G. Evans (2006), Channel head location and characteristics using digital elevation models, *Earth Surf. Processes Landforms*, 31(7), 809–824.
 Helmsen, J., E. G. Puckett, P. Collela, and M. Dorr (1996), Two new methods for simulating photolithography development in 3-D, *Proc. SPIE Int. Soc. Opt. Eng.*, 2726, 253–261.
 Howard, A. D. (1994a), A detachment-limited model of drainage basin evolution, *Water Resour. Res.*, 30(7), 2261–2285.
 Howard, A. D. (1994b), Badlands, in *Geomorphology of Desert Environments*, edited by A. D. Abrahams and A. J. Parsons, pp. 213–242, Chapman and Hall, New York.
 Howard, A. D. (1997), Badland morphology and evolution: Interpretation using a simulation model, *Earth Surf. Processes Landforms*, 22, 211–227.
 Kimmel, R. (2003), *Numerical Geometry of Images: Theory, Algorithms, and Applications*, 209 pp., Springer, New York.
 Kirkby, M. J. (1984), Modeling cliff development in South Wales: Savigear re-reviewed, *Z. Geomorphol.*, 28, 405–426.
 Kirkby, M. J. (1985), A model for the evolution of regolith-mantled slopes, in *Models in Geomorphology*, edited by M. J. Woldenberg, pp. 213–237, Allen and Unwin, Winchester, Mass.

- Koenderink, J. (1984), The structure of images, *Biol. Cybern.*, 50(5), 363–370.
- Lashermes, B., E. Foufoula-Georgiou, and W. E. Dietrich (2007), Channel network extraction from high-resolution topography using wavelets, *Geophys. Res. Lett.*, 34, L23S04, doi:10.1029/2007GL031140.
- Mark, D. M. (1988), Network models in geomorphology, in *Modeling Geomorphological Systems*, edited by M. G. Anderson, pp. 73–97, John Wiley, New York.
- McKean, J., and J. J. Roering (2004), Objective landslide detection and surface morphology mapping using high-resolution airborne laser altimetry, *Geomorphology*, 57, 331–351, doi:10.1016/S0169-555X(03)00164-8.
- McMaster, K. J. (2002), Effects of digital elevation model resolution on derived stream network positions, *Water Resour. Res.*, 38(4), 1042, doi:10.1029/2000WR000150.
- McNamara, J. P., A. D. Ziegler, S. H. Wood, and J. B. Vogler (2006), Channel head locations with respect to geomorphologic thresholds derived from a digital elevation model: A case study in northern Thailand, *For. Ecol. Manage.*, 224, 147–156.
- Memoli, F., and G. Sapiro (2005), Distance functions and geodesics on submanifolds of R^d and point clouds, *SIAM J. Appl. Math.*, 65(4), 1227–1260.
- Montgomery, D., and W. E. Dietrich (1988), Where do channels begin?, *Nature*, 336, 232–234, doi:10.1038/336232a0.
- Montgomery, D. R., and W. E. Dietrich (1989), Source areas, drainage density, and channel initiation, *Water Resour. Res.*, 25(8), 1907–1918.
- Montgomery, D. R., and W. E. Dietrich (1992), Channel initiation and the problem of landscape scale, *Science*, 255, 826–830.
- Montgomery, D. R., and W. E. Dietrich (1994), Landscape dissection and drainage area-slope thresholds, in *Process Models and Theoretical Geomorphology*, edited by M. J. Kirkby, pp. 221–246, John Wiley, New York.
- Montgomery, D., and E. Foufoula-Georgiou (1993), Channel network source representation for digital elevation models, *Water Resour. Res.*, 29(12), 3925–3934.
- Mumford, D., and J. Shah (1989), Optimal approximation by piecewise smooth functions and associated variational problems, *Commun. Pure Appl. Math.*, 42, 577–685.
- O’Callaghan, J., and D. Mark (1984), The extraction of drainage networks from digital elevation data, *J. Comput. Vis. Graph. Image Process.*, 28(3), 323–344.
- Perona, P., and J. Malik (1990), Scale-space and edge detection using anisotropic diffusion, *IEEE Trans. Pattern Anal. Mach. Intel.*, 12(7), 629–639.
- Roering, J. J., J. Kirchner, and W. E. Dietrich (1999), Evidence for non-linear, diffusive sediment transport on hillslopes and implications for landscape morphology, *Water Resour. Res.*, 35(3), 853–870.
- Sapiro, G. (2001), *Geometric Partial Differential Equations and Image Analysis*, 412 pp., Cambridge Univ. Press, New York.
- Sethian, J. A. (1999), *Level Set Methods and Fast Marching Methods*, 400 pp., Cambridge Univ. Press, Cambridge, U. K.
- Smith, M. J., J. Rose, and S. Booth (2006), Geomorphological mapping of glacial landforms from remotely sensed data: An evaluation of the principal data sources and an assessment of their quality, *Geomorphology*, 76, 148–165, doi:10.1016/j.geomorph.2005.11.001.
- Solé, A., V. Caselles, G. Sapiro, and F. Arándiga (2004), Morse description and geometric encoding of digital elevation maps, *IEEE Trans. Image Process.*, 13(9), 1245–1262.
- Staley, D. M., T. A. Wasklewicz, and J. S. Blaszczynski (2006), Surficial patterns of debris flow deposition on alluvial fans in Death Valley, CA using airborne laser swath mapping, *Geomorphology*, 74, 152–163.
- Tarboton, D. G. (1997), A new method for the determination of flow directions and contributing areas in grid digital elevation models, *Water Resour. Res.*, 33(2), 309–319.
- Tarboton, D. G., R. L. Bras, and I. Rodriguez-Iturbe (1988), The fractal nature of river networks, *Water Resour. Res.*, 24(8), 1317–1322.
- Tarboton, D. G., R. L. Bras, and I. Rodriguez-Iturbe (1989), The analysis of river basins and channel networks using digital terrain data, *Rep. 326*, Ralph M. Parson Lab., Dep. of Civ. Eng., Mass. Inst. of Technol., Cambridge, Mass.
- Tarboton, D. G., R. L. Bras, and I. Rodriguez-Iturbe (1991), On the extraction of channel networks from digital elevation data, *Hydrol. Processes*, 5(1), 81–100.
- Tarolli, P., and G. Dalla Fontana (2009), Hillslope to valley transition morphology: New opportunities from high resolution DTMs, *Geomorphology*, 113, 47–56.
- Tarolli, P., and D. G. Tarboton (2006), A new method for determination of most likely landslide initiation points and the evaluation of digital terrain model scale in terrain stability mapping, *Hydrol. Earth Syst. Sci.*, 10(5), 663–677.
- Tribe, A. (1991), Automated recognition of valley heads from digital elevation models, *Earth Surf. Processes Landforms*, 16(1), 33–49.
- Tribe, A. (1992), Automated recognition of valley lines and drainage networks from grid digital elevation models: A review and a new method, *J. Hydrol.*, 139, 263–293.
- Tsai, Y. R., L. T. Cheng, S. Osher, and H. K. Zhao (2003), Fast sweeping algorithms for a class of Hamilton-Jacobi equations, *SIAM J. Numer. Anal.*, 41(2), 673–694.
- Tsitsiklis, J. N. (1995), Efficient algorithms for globally optimal trajectories, *IEEE Trans. Autom. Control*, 40(9), 1528–1538.
- Vianello, A., M. Cavalli, and P. Tarolli (2009), Lidar-derived slopes for headwater channel network analysis, *Catena*, 76, 97–106.
- Witkin, A. P. (1983), Scale-space filtering, paper presented at 10th International Joint Conference on Artificial Intelligence, ACM Inc., New York.
- Yatziv, L., A. Bartesaghi, and G. Sapiro (2006), O(N) implementation of the fast marching algorithm, *J. Comput. Phys.*, 212, 393–399.
- Zhao, H. K. (2004), A fast sweeping method for Eikonal equations, *Math. Comput.*, 74(250), 603–627.

W. E. Dietrich, Department of Earth and Planetary Science, University of California, Berkeley, CA 94720, USA.

T. Do Trung, Département de Mathématiques, École Normale Supérieure de Cachan, Bâtiment Laplace 1er étage, 61 Ave. du Président Wilson, F-94235 Paris, Cachan CEDEX, France.

E. Foufoula-Georgiou and P. Passalacqua, Saint Anthony Falls Laboratory, National Center for Earth Surface Dynamics, Department of Civil Engineering, University of Minnesota, 2 3rd Ave. SE, Minneapolis, MN 55414, USA. (efi@umn.edu)

G. Sapiro, Department of Electrical and Computer Engineering, University of Minnesota, 200 Union St. SE, Minneapolis, MN 55455, USA.